Pool Fires Within a Large Under-Ventilated Environment: Experimental Analysis and Numerical Simulation Using OpenFOAM

Marco Cavazzuti (ID) **, Dipartimento di Scienze e Metodi dell'Ingegneria, Università degli Studi di Modena e Reggio Emilia, Via Giovanni Amendola 2, 42122 Reggio Emilia, Italy*

Paolo Tartarini, Dipartimento di Ingegneria "Enzo Ferrari", Università degli Studi di Modena e Reggio Emilia, Via Pietro Vivarelli 10, 41125 Modena, Italy

Abstract. Experimental analyses and numerical simulations are carried out on a test case involving an heptane pool fire within a large under-ventilated environment. During the experiments, the temperature history at several locations within the room is monitored by means of thermocouples, and the fire radiative heat transfer estimated through a plate thermocouple. The experimental layout is then replicated numerically and tested using OpenFOAM CFD code. The study is a preliminary analysis performed for code validation purposes on a full-scale fire scenario. The results of the simulations are compared to the experimental results and critically analysed, finding a reasonable agreement overall. Critical issues in fire modelling are also highlighted. In fact, due to the problem complexity and the limitations of the numerical models available some important aspect that can significantly influence the outcome of the simulations must be calibrated a posteriori, somewhat limiting the general predictive applicability of the fire models. Primarily, these are the heat release rate history, the combustion efficiency, and, to a lesser extent, the convective heat transfer boundary condition at the wall.

1. Introduction

Fire simulation is a challenging task since it requires the modeling of difficult physical and chemical processes ranging from turbulent buoyant convection and radiative heat transfer to chemical kinetics for combustion, pyrolysis, and soot formation.

Over the last few years the increase in performances of modern computers is shifting the attention from simpler zone models to more elaborated field models.

---

* Correspondence should be addressed to: Marco Cavazzuti, E-mail: marco.cavazzuti@unimore.it

In a field of investigation like fire safety engineering where recurring to experiments is often very expensive, if viable at all, the chance to rely on simulations is certainly welcomed. However, much attention and a thorough validation are needed for the correct setup of such simulations, as they are characterised by a number of complex physical models.

In the literature, several papers have been published on these issues using different simulation means, focusing on different fire scenarios, or discussing the development and validation of various submodels (e.g. for turbulence, radiation, pyrolysis or soot formation) to be embedded into the field models. In these studies, the field model employed is, in most cases, the fire dynamics simulator (FDS) developed by NIST, while more recently also the CFD solver FireFOAM included in the OpenFOAM package has attracted interest.

Earlier works usually adopt the k-ε turbulence model in conjunction with eddy break-up (EBU) combustion models, while radiation is not always accounted for explicitly. For instance, in [1] time-dependent instabilities in large pool fires in stagnant atmosphere are addressed finding a good agreement between the numerical and the experimental frequency of the instabilities caused by vortex shedding at the fire base, while [2] compares different combustion models on a few test cases involving enclosure and tunnel fires. It is highlighted how these fail to give consistent accurate predictions, in terms of temperature distribution, for all the possible scenarios.

In the following years many works dealt with pool fires in medium scale compartments, gradually abandoning k-ε turbulence modeling in favour of large eddy simulation (LES). These focus either on turbulent fluctuations of temperature and velocity [3], or CFD validation versus experiments [4]. Various methods are proposed for improving turbulence prediction, such as dynamically adjusting the model coefficients on the basis of the local conditions [5]. The first works accounting for soot formation appeared, going from simple models assuming a given volume fraction of fuel is turned into soot during combustion [6], to more complex and computationally expensive models for tracking soot formation and burnout through nucleation, coagulation, surface growth, and oxidation [7, 8], or using a partially stirred reactor model for soot formation and oxidation [9]. Similarly, concerning radiation heat transfer modeling, different approaches are found ranging from simple models assuming a constant fraction of the heat generated is lost through radiation [10], to more standard models such as P-1 and discrete ordinates method (DOM). Attention must be devoted also to radiation absorption by the medium where weighted-sum-of-gray-gases models [11] or more complex band models of the radiation spectrum [12] have been proposed. Models to account for the interaction between turbulence and radiation are also discussed in [13, 14]. With regard to combustion, the simpler EBU model is gradually being substituted by eddy dissipation concept (EDC) approach [15] providing better estimates of the reaction rate, or by much more complicated and computationally intensive flamelet models [16].

While most of the studies assume a constant burning rate in the simulation [17], in [18] it is stressed out how during pool fire experiments the burning rate is not constant, and a transient inlet boundary condition should rather be adopted. The

fact is that this condition is not known *a priori* and can only be derived from experiments (e.g. by attaching a load cell to the pool), even though some theoretical formulation has been attempted [19, 20]. This is a major deficiency in combustion modelling and for this reason several works raise a warning on the limited applicability of field models. Although their use is spreading, further development and calibration is needed, and in [21] it is argued that complex field models may still be overperformed by much simpler zone models.

More recent numerical works mostly deal with code validation against experiments on several typical benchmark test cases, among which: purely buoyant plumes [22], ventilated [23], and under-ventilated [24] fires in medium and full-scale enclosures. The first works based on OpenFOAM also appeared after the introduction of FireFOAM solver [25], as well as the first comparisons between FDS 5 and OpenFOAM. A comparison made on buoyant plume simulations [26] states that the first overperforms the latter in terms of streamwise velocity and fuel mass fraction predictions, while the latter is able to give better results in terms of air entrainment, cross-stream velocity, and flame puffing frequency.

Another comparison between FDS 4 and FireFOAM is provided in [27] on a small size methane diffused burner flame without soot modelling, with the former better predicting the mixture fraction, and the latter better capturing the temperature field. It is highlighted how a single step reaction with no soot modelling may yet be inadequate in case of combustion of heavier fuels.

In [28] a novel sprinkler dispersion model is proposed and validated against experimental results using FireFOAM finding excellent agreement. Given that the study focuses on spray models alone, no actual fire is modelled. In [29] the same solver is used to calibrate a composite materials pyrolisis model against experimental results, and in [30] to model combustion in an electric vehicle battery following a cell overheat. The heat release rate (HRR) is taken from experiments, and electrolyte combustion activated once a threshold temperature is reached in the cell.

Concerning the numerical setup, due to the fact that field models have reached a high level of complexity, the best trade-off between accuracy and computing time is still an open question, and of course the choice of the submodels adopted in the simulations varies greatly among the different works. Table 1 summarizes into a synoptic table the state-of-the-art in fire modeling by listing, in order of complexity, the most common choices found in numerical works in the literature.

An important issue concerning combustion modeling is that for computational reasons, due to the degree of complexity of the simulations and the large mesh required by full-scale analyses, it is almost impossible to rely on computationally expensive and more accurate models. EBU combustion model assuming one step infinitely fast chemistry or, at most, EDC models with a limited number of reaction mechanisms are generally accepted under the assumption of fixed quantity soot production and radiative heat transfer. This can become a problem when addressing under-ventilated fire conditions where severely high yield of soot and carbon monoxide are found due to incomplete combustion. In fact, one step EBU model is not able to account for incomplete combustion, leading to an overestimation of the flame temperature and of the HRR. Further, such a simple model is

Table 1
Common Choices in Fire Modeling Setup, the Most Commonly Used are Highlighted in Italic

Model	Choices
Turbulence	Buoyancy modified k-ε; *LES*
LES SGS treatment	One-equation; Smagorinsky; dynamic Smagorinsky
Combustion	Non-reacting thermal elements; EBU; *EDC*; flamelet
Radiative heat transfer	None; P-1; *DOM*
Emission and absorption	Fixed quantity; *weighted-sum-of-gray-gases*; absorption bands
Soot formation	None; *fixed quantity*; Arrhenius law; detailed chemistry

unable to predict fire extinguishment, as highlighted in [31], and soot formation rate can only be guessed.

Concerning pool fires in enclosures with controlled ventilation, the literature focuses mostly on discriminating between different combustion regimes, such as well-ventilated or fuel-controlled, in case the oxygen abounds, and under-ventilated or ventilation-controlled, in case the oxygen is limited. In [32] an analytical model based on the well-stirred reactor model and on conservation equations is presented. It is highlighted how the fire regime and the combustion time are of course controlled by ventilation, but also by an additional factor accounting for the quantity of oxygen in the room with respect to that needed for the complete combustion of the fuel. In [33], starting from similar concepts, suitable scaling parameters are discussed for the construction of reduced-scale experiments for the case of mechanically ventilated confined fires. In [34] instabilities in the combustion rates occurring in strongly under-ventilated combustions are investigated experimentally, while in [35] pool fires in elongated enclosures such as corridors are analysed finding how ventilation tends to be less efficient with these geometries. Numerical analyses are less common. In [24] a medium-scale enclosure is investigated using FDS, the analysis includes an EBU combustion model and a soot formation model, and focuses on the different fire regimes encountered as the oxygen in the room is depleted. In [36] a flame extinction model based on the Damköhler number is proposed and is tested using FireFOAM. In [37] and [38] FDS, versions 5 and 6.7 respectively, is used to investigate the different combustion regimes in fires within an enclosure with a single opening. In the former the focus is on temperature and velocity fields for different heat release rates, while in the latter a criterion to discriminate between the regimes is proposed. It is highlighted how FDS fails to deal with incomplete combustion.

In this paper, experiments of a pool fire in an under-ventilated large environment are discussed. The experimental layout is then modelled and numerically simulated using FireFOAM as implemented in OpenFOAM 8 version (to be noted that in most recent OpenFOAM versions FireFOAM solver has been merged into buoyantReactingFOAM, a solver having similar modelling capabilities). The results of the simulations are compared to the experimental results in terms of temperature distributions for validation purposes and critically analysed. The goal

is to present an introductory study on the capabilities of OpenFOAM in modeling a fire in a full-scale under-ventilated environment. The experiments were carried out in a laboratory with limited equipment availability. In the authors opinion numerical models for fire simulation are indeed useful although still affected by limits that may question their practical applicability to real fire cases of concern in fire safety engineering applications if detailed predictions are sought.

2. Experimental test Case Setup

Experiments were conducted at Bettati Antincendio srl in a dedicated metal sheet garage having a 5.3 m×5.3 m base section and a pitched roof 3.5 m high at the room centre and 3.0 m high at the sides. Access to the garage was granted through a large door 2.9 m high and 3.0 m wide. The overall room volume was 91.3 m³. A plexiglass spyhole was obtained at the base of a side wall allowing the visualization and recording of the flame with a camera during the experiment.

A special foam was spread at the metal sheet junctions to limit diffuse smoke leakages out of the room. This is a REI 180 fire resistant polyurethane foam (commercial name, Soudafoam FR).

The 0.5 m×0.5 m pool was placed in the centre of the room and filled with 20 l of water and 5 l of fuel so that the free surface in the pool was located 10 cm above the ground level, close to the pool rim. The water was used to protect the floor beneath the pool from overheating. At the room centre, 1 m above the ground, a 2.0 m×1.5 m steel panel 3 mm thick was mounted on two trestles. The presence of the panel is due to the fact that in successive experiments the fire extinguishing performance of a water mist nozzle mounted on the garage roof had to be tested in a scenario in which the fire was hidden from view to the sprinkler. It is expected that the panel will absorb and re-radiate a minor portion of the combustion heat, its surface being touched by the flame.

14 thermocouples were placed at several locations inside the room according to Figure 1 and Table 2 to monitor sensible locations such as the flame region, the area around the panel, the room centre, and the walls at different heights. These are bare-bead K type thermocouples (Q/TW-20-KK model) with 0.8 mm glass fiber insulated wires, resistant up to 704°C.

In particular, 8 thermocouples were mounted in a grid-like fashion on the $y = 0$ m plane recording the temperature history at three heights on the side wall (TC 8–10), next to the panel (TC 3–5), and at the room centre (TC 6–7). 3 thermocouples were located in the persistent flame region slightly above the pool free surface (TC 1, 11), and between the pool and the panel in the intermittent flame region (TC 2). Two additional thermocouples were mounted in front of and behind the panel at $z = 3$ m (TC 12-13). Finally a 10 cm×10 cm plate thermocouple (PTC 1) was placed in front of the flame, 1.6 m far from the room centre and 0.5 m from the ground. This thermocouple allows the evaluation of the flame radiation and HRR history, as will be discussed in the following. Thermocouples were connected to a NI-4351 multimeter with TBX-68T terminal block recording the temperature every 11 s.
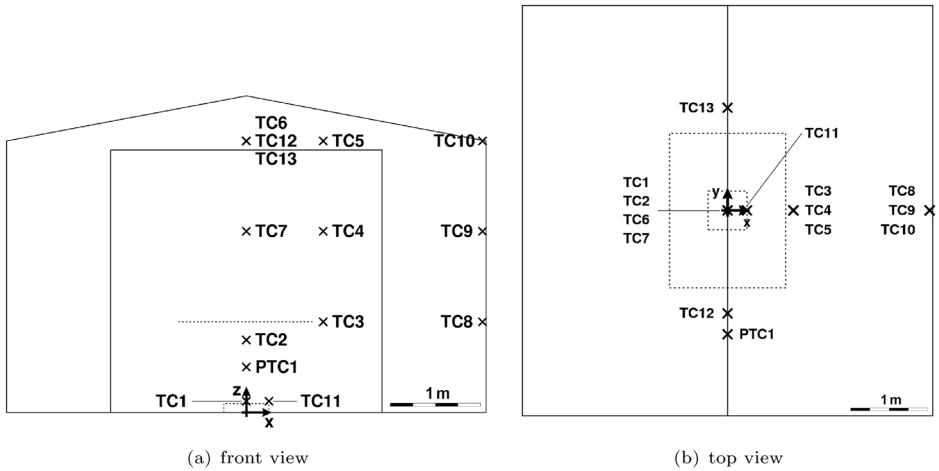
(a) front view   (b) top view

Figure 1.   Garage layout and thermocouples arrangement.

Table 2
Experimental Thermocouples Arrangement, Coordinates are Given with Respect to the Axis System in Figure 1

Thermocouple	Coordinates [m]			Notes
	x	y	z	
TC 1	0.0	0.0	0.12	Central, above the pool free surface
TC 2	0.0	0.0	0.8	Central, below the steel panel
TC 3	0.85	0.0	1.0	Right of the panel, 1 m from the ground
TC 4	0.85	0.0	2.0	Right of the panel, 2 m from the ground
TC 5	0.85	0.0	3.0	Right of the panel, 3 m from the ground
TC 6	0.0	0.0	3.0	Central, 3 m from the ground
TC 7	0.0	0.0	2.0	Central, 2 m from the ground
TC 8	2.63	0.0	1.0	At the side wall, 1 m from the ground
TC 9	2.63	0.0	2.0	At the side wall, 2 m from the ground
TC 10	2.63	0.0	3.0	At the side wall, 3 m from the ground
TC 11	0.25	0.0	0.12	Right of the pool, above the free surface
TC 12	0.0	−1.33	3.0	In front of the panel, 3 m from the ground
TC 13	0.0	1.33	3.0	Behind the panel, 3 m from the ground
PTC 1	0.0	−1.6	0.5	In front of the panel 0.5 m from the ground

It must be noted that the thermocouples employed were non-shielded, thus the ones located in the flame region are expected to return erroneous readings and are mainly used for the purpose of evaluating the time at which fire extinguishment occurs. The camera placed in front of the spyhole in fact is of no help to this purpose due to the large amount of smoke produced during combustion that covered completely the flame from sight after ≈4 minutes since the pool fire was lit.

The liquid fuel used for the fire was a mixture with 90% in volume of n-heptane (C_7H_{16}) and 10% of methyl acetate ($C_3H_6O_2$).

3. Numerical Setup

The pool fire experiment was reproduced numerically using FireFOAM. This solver is based on LES turbulence modeling with one step EBU combustion. Such a combustion model is a very simple one. It is based on the assumption of infinitely fast chemistry, with no soot formation model, and is unable to predict flame extinction as it may occur in a strongly under-ventilated environment due to lack of oxygen. One equation model is adopted for sub-grid scale (SGS) treatment, and DOM with gray mean absorption and emission model for radiative heat transfer. Soot formation is not modeled, and the pyrolysis model turned off since no pyrolysis occurs in our case study.

Unity Lewis number is assumed, since turbulent Prandtl and Schmidt numbers are set to 0.5, as commonly found in the literature. Smagorinsky constant [39]

$$C_s = \left(\frac{C_k^3}{C_\varepsilon}\right)^{\frac{1}{4}} \tag{1}$$

is set to 0.168, being $C_k = 0.094$ and $C_\varepsilon = 1.048$.

Euler scheme is used for time discretization, and Gauss linear scheme for gradient and divergence spatial discretization. Time stepping is adaptive and chosen so that the maximum Courant number is 0.5.

The steel panel is modeled as a thin surface having 3 mm thickness, $7850 \, kg/m^3$ density, $16.3 \, W/m \, K$ thermal conductivity, and $502 \, J/kg \, K$ specific heat. These values are assumed constant also considering their marginal change with temperature. The overall panel weight is 70.6 kg.

3.1. The Mesh

The mesh used for the simulations is fully hexahedral and composed of 809 thousand elements ($106 \times 106 \times 72$), with average cell size of 48 mm (Figure 2(a)). The mesh is mostly uniform in size except near the inlet and outlet sections where it thickens slightly, and is created by extrusion in the y direction. Two additional grids were tested for mesh independency check: a smaller one with 376 thousand elements ($82 \times 82 \times 56$) and average cell size of 62 mm, and a larger one with 2356 thousand elements ($152 \times 152 \times 102$) and average cell size of 34 mm. The temperature histories found at the thermocouple locations during preliminary runs are in good agreement between the different grids, the thicker mesh better reproducing the shape of the temperature peaks in the flame region, and the thinner one deviating at times from the others. Figure 2(b) compares the three grids in terms of temperature history recorded during the first 100 s at TC 4 where the worst match is found. Concerning the computing times, the simulation of the first 100 s took
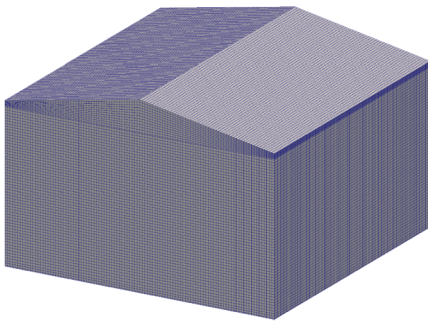
(a) View of the mesh used for the simulations
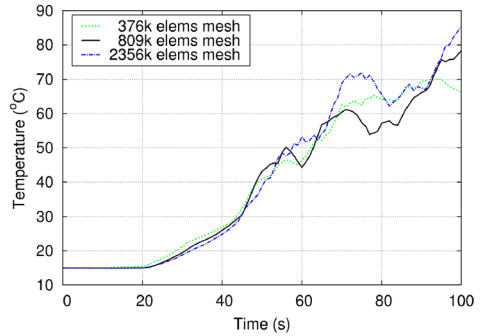
(b) Mesh independency test: temperature history at TC 4

Figure 2. The mesh and the mesh independency test.

approximately 2.5, 6, and 22 days for the grids tested, running on a 4-CPU workstation equipped with Intel i7-2600 CPU at 3.4 GHz.

At first, when the HRR is still small and the flame stable, the temperature history at TC 4 is the same for the three grids. As the fire grows, instabilities prevail and the flame begins to sway in space. TC 4, being located slightly above the panel on its right side, is particularly affected by the flame instability so that the temperature history becomes quickly irregular showing peaks and valleys as the flame tilts in one direction or another. The coarser mesh appears less able to catch these oscillations due to the larger diffusion that flattens the irregularities. Intermediate and finer grids, instead, showing similar oscillation amplitudes and frequencies, even though with small temperature and time offsets, are deemed more suitable for the simulations. Nonetheless, the temperature trend among the three grids is comparable.

For the simulations the choice fell on the 809 thousand elements mesh, as a good compromise between accuracy and computing time. Being a fully hexahedral grid, its quality is very high and is characterised by maximum skewness of 1.5 and maximum non-orthogonality of 39° as evaluated by OpenFOAM.

To properly resolve the large-scale structures in fire plumes analysis, it is suggested in the literature [24, 25] to choose a mesh with at least ten elements within the fire characteristic length scale, which is defined as

$$L^* = \left(\frac{\dot{Q}}{\rho_\infty T_\infty c_\mathrm{p} \sqrt{g}} \right)^{\frac{2}{5}} \tag{2}$$

where L^* is expressed in m, $\dot{Q}$ is the HRR expressed in W, ρ_∞ and T_∞ the air density and temperature away from the fire expressed in kg/m^3 and K respectively, c_p the specific heat in J/kg K, and g the gravitational acceleration constant in m/s^2.

Considering the operating conditions of the simulations, this confirms the suitability of the chosen mesh above an HRR of 195 kW, a situation which is always attained in the simulations except for a short period at the very beginning of the

combustion process, or unless the combustion efficiency becomes particularly low, as will be shown in the following. This limit would grow to 335 kW for the coarser mesh, and would drop to 75 kW for the finer mesh.

3.2. *Fuel and Combustion*

As mentioned, the liquid fuel used in the pool fire is a 90%/10% mixture in volume of n-heptane and methyl acetate. Table 3 summarizes the fuel properties and the quantities involved in the present study. The gas phase volume and density are computed according to the ideal gas state equation, assuming the atmospheric temperature and pressure at the time of the experiments: 15°C and 1.006 bar. The lower heating value (LHV) of the fuel components reported has already been reduced by the heat of vaporization in order to account for the liquid to gas phase change not modelled numerically.

   Due to the fact that the solver only allows one reaction mechanism to be defined, an equivalent amount of n-heptane is assumed in the simulations so that the Total Heat Release (THR) is the same that can be derived from Table 3 for the mixture, i.e. THR = 146.2 MJ. This corresponds to an overall n-heptane mass of 3.28 kg. The reaction mechanism imposed is the following

$$C_7H_{16} + 11\,O_2 + 41.00\,N_2 \rightarrow 7\,CO_2 + 8\,H_2O + 41.00\,N_2 + 4.47\frac{MJ}{mol}, \qquad (3)$$
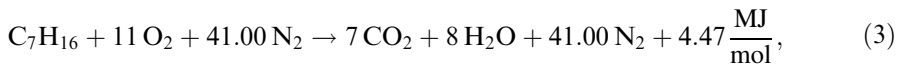
resulting in an oxygen consumption of 11.5 kg overall. This holds under the hypothesis of complete combustion. However, it is known that in under-ventilated fires complete combustion is not attained since a large amount of carbon monoxide and soot is generated. In moderately under-ventilated fires combustion inefficiencies can account for the loss of up to 60% of the theoretical heat released [24], while according to [10] even in case of well-ventilated fires more than 20% of the fuel mass can be turned into soot. As the equivalence ratio grows, fire extinction may even occur [33, 36]. The amount of fuel that is turned into soot or into carbon monoxide depends on many parameters and is not known a priori. As a consequence, the impact that combustion inefficiencies have on the HRR is unknown too. Nonetheless, considering that the amount of oxygen in the room at ambient conditions can be estimated in 25.3 kg and that a non-negligible fraction will leak out of the garage as the temperature in the room grows, it is apparent that the fire will develop in a progressively under-ventilated environment. This conclusion is also in line with the criteria outlined in [32] for discriminating among different fire regimes in poorly-ventilated conditions.

   For this reason, and since no soot formation model is available in the solver, simulations are repeated also for two different reaction mechanisms as follows
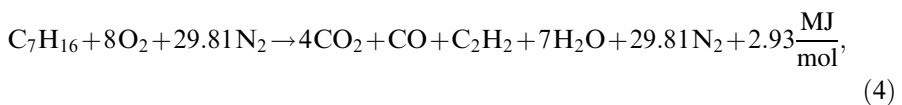
$$C_7H_{16} + 8O_2 + 29.81N_2 \rightarrow 4CO_2 + CO + C_2H_2 + 7H_2O + 29.81N_2 + 2.93\frac{MJ}{mol},$$

$$(4)$$

Table 3
Fuel Properties and Quantities Involved

	Liquid state		Gas state			Properties		
Component	Volume [dm^3]	Density [kg/m^3]	Volume [m^3]	Density [kg/m^3]	Constant [J/kg K]	Mass [kg]	Molar Mass [kg/kmol]	LHV [MJ/kg]
C_7H_{16}	4.5	679.5	0.7267	4.208	82.97	3.058	100.210	44.60
$C_3H_6O_2$	0.5	932.0	0.1498	3.111	112.24	0.466	74.078	21.09
Mixture	5.0	704.8	0.8765	4.020	86.84	3.524	95.744	41.49

$$C_7H_{16} + 5O_2 + 18.64N_2 \rightarrow CO_2 + 2CO + 2C_2H_2 + 6H_2O + 18.64N_2 + 1.39\frac{MJ}{mol}.$$

(5)
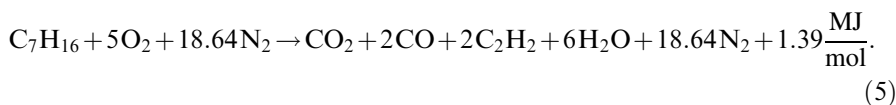
In these reactions it is arbitrarily supposed that from the combustion of an heptane molecule one (or two) molecules of carbon monoxide and acetylene are produced. These formally stand for incomplete combustion (formation of CO) and soot formation (formation of C_2H_2). Acetylene, in fact, is considered a soot precursor specie in that, without entering into further chemical details, it represents the basic element from which polycyclic aromatic hydrocarbons forming soot are created.

In the first reaction it is assumed that 12% of the fuel mass undergoes incomplete combustion, 25% is turned into soot, and the combustion efficiency is 66% (i. e. THR = 95.8 MJ). In the second reaction it is assumed that 24% of the fuel mass undergoes incomplete combustion, 50% is turned into soot, and the combustion efficiency is 31% (i.e. THR = 45.5 MJ). Even though this value may seem very low, in strongly under-ventilated environments such a situation may not be too far from reality towards the end of the combustion process when oxygen shortage will occur.

The stoichiometric air-to-fuel ratio is 15.2 for the first reaction, 11.1 for the second, 6.9 for the last. Air is assumed to be a mixture as in Table 4, where the amount of water vapor corresponds to an 85% relative humidity at the temperature of 15 °C.

An estimate of the combustion efficiency in under-ventilated pool fires can be given using the method outlined in [40] where the plume equivalence ratio is evaluated from temperature measurements in the flame region and in the room, and from oxygen concentration data using the formula proposed in [41], and fed into the formula proposed in [42] for the combustion efficiency. By averaging these data in time using the temperature readings from the experiments and the oxygen concentration from the simulations, an average combustion efficiency of ≈64% can be estimated, which agrees well with the reaction mechanism hypothesized in Eq. (4).

Table 4
Air Composition

Component	Volume Fraction [%]	Mass Fraction [%]
N_2	76.974	74.838
O_2	20.649	22.931
Ar	0.921	1.277
CO_2	0.035	0.054
H_2O	1.439	0.900

3.3. Inlet Boundary Condition

It is found that in three runs of the experiments different burning times are attained before the fuel is depleted and the fire extinguishes. After each experimental run, the complete consumption of the fuel is checked: trying to lit the pool again after the room has been aerated always resulted in no fire. Even though this does not necessarily mean all the fuel underwent combustion, at least it makes us confident most did. In fact, even though the fire is located in an almost closed environment, the room is large enough so that oxygen should be found, in theory, to allow for the combustion of the whole amount of fuel poured into the pool even in case the reaction mechanism in Eq. (3) is assumed.

As exact experiment repeatability is not attained easily, the average fuel flow rate and HRR vary from time to time. This is due to a number of non-controllable factors interfering with the experiments such as, for instance, the environment temperature, its humidity, and the wind. For the choice of the fuel flow rate at the pool surface to be adopted in the simulations we refer to an experimental run in which the flame extinguished in 379 s. This results in an average fuel mass flow rate of 8.65 g/s, corresponding to an average HRR of 386 kW in case of complete combustion. In the additional experimental tests the flame extinguishment always occurred in a time range between 5.5 min and 6.5 min while the temperature trends recorded by the thermocouples were self-similar across all the tests performed.

The choice of a proper inlet boundary condition is not straightforward since the flame HRR is not constant over time. Thus, assuming constant fuel mass flow rate can lead to erroneous temperature predictions, and this is particularly true at the early stages of fire development. The measurement of the pool mass loss rate over time would have been easier with the use of a load balance system. Such an instrument was not available at the time of the experiments so that the HRR history had to be estimated by other means.

An approximate esteem is extrapolated from PTC 1, TC 1, and TC 2 data. This is then adopted as inlet boundary condition in the simulations performed. From the temperature readings of the plate thermocouple PTC 1, following [43], it is possible to resolve the incident thermal radiation on the plate under the assump-
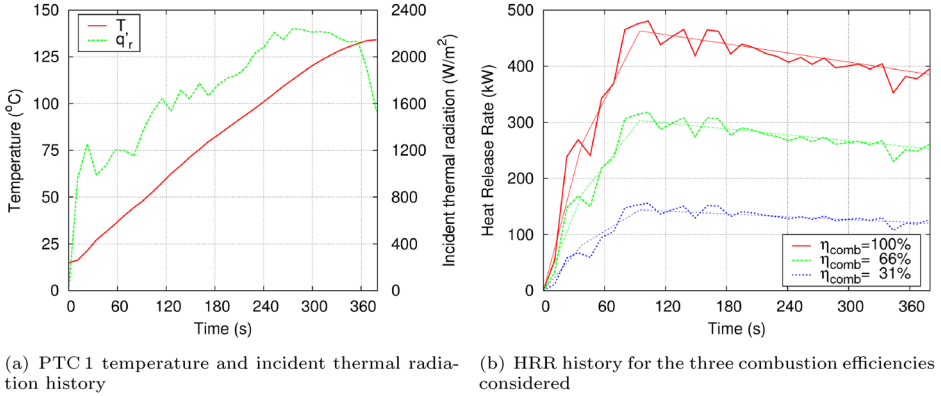
(a) PTC 1 temperature and incident thermal radiation history

(b) HRR history for the three combustion efficiencies considered

Figure 3. Data extrapolated from PTC 1 readings.

tion of gray radiation. Figure 3a shows the temperature (T) and the incident thermal radiation history ($\dot{q}_r$) on the plate thermocouple PTC 1.

The amount of heat that is transferred in form of thermal radiation from the flame to the environment (Q_r) during the whole combustion process under the assumption of isotropic radiation can be estimated integrating the incident thermal radiation in time and multiplying for the surface of a sphere of radius r equal to the distance between the pool centre and the plate thermocouple

$$Q_r(t) = 4\pi r^2 \int_0^t \dot{q}_r(t)\mathrm{d}t\,. \tag{6}$$

Considering the distance between the plate thermocouple and the pool, the isotropic assumption is acceptable. According to Eq. (6), at the end of the combustion process $Q_r(t_{\mathrm{end}}) = 21.0\,\mathrm{MJ}$.

Let us consider the HRR at a time t as given by two terms, the radiative thermal power $\dot{Q}_r(t)$ proportional to T^4, and the convective thermal power $\dot{Q}_c(t)$ in the neighbourhood of the flame proportional to T

$$\mathrm{HRR}(t) = \dot{Q}_r(t) + \dot{Q}_c(t) = c_r\left(T_{\mathrm{flame}}^4(t) - T_{\mathrm{room}}^4(t)\right) + c_c\left(T_{\mathrm{flame}}(t) - T_{\mathrm{room}}(t)\right) \tag{7}$$

where c_r and c_c are generic coefficients to be determined. A detailed account of the heat transfer coefficients, the surface areas and emissivities are out of reach considering the experimental data available. Nonetheless, the two coefficients can be adapted in order to tune $\dot{Q}_r(t)$ and $\dot{Q}_c(t)$ so that their integrals over the combustion time matches with the given values. In particular, we want the overall heat transferred through radiation to be equal to $21.0\,\mathrm{MJ}$ as mentioned, and the overall heat transferred through convection $Q_c(t_{\mathrm{end}})$ to account for the rest of the heat released (e.g. $125.2\,\mathrm{MJ}$ in case of complete combustion).

Table 5
Nodes of the Piecewise Linear Fuel Mass Flow Rate and HRR History Assumed in the Simulations

Time [s]	Fuel flow rate [g/s]	Heat release rate [kW]		
		$\eta_{comb} = 100\%$	$\eta_{comb} = 66\%$	$\eta_{comb} = 31\%$
0.0	0.00	0.0	0.0	0.0
37.9	5.88	262.3	172.0	81.6
94.8	10.38	462.9	303.4	144.0
378.5	8.65	385.8	252.9	120.0
379.5	0.00	0.0	0.0	0.0

Repeating for the three combustion efficiencies considered in this study, the HRR histories in Figure 3(b) are found. The reference values used in Eq. (7) for $T_{flame}(t)$ and $T_{room}(t)$ are the maximum value among those recorded by the thermocouples in the flame region (TC 1 and TC 2), and the value recorded at PTC 1 respectively.

The HRR histories in Figure 3b are approximated, for simulation purposes, by linear piecewise functions as reported with thinner lines in the figure. According to these curves, the 68% of the average HRR is reached after 10% of the combustion time. The HRR then grows at 120% compared to its average after 25% of the time, to be reduced at 100% at the end of the combustion process. This function fits reasonably well all the three cases, regardless of the combustion efficiency (see Table 5).

Considering the lower combustion efficiency cases, which are expected to compare better to the experimental results, it is found that radiative heat transfer should globally account between 22% and 46% of the THR respectively. These values are in line with the assumptions made in several papers in the literature. For instance, [25] and [10] perform simulations without modeling explicitly the radiative heat transfer, but assuming that 20% of the heat generated by the combustion process is lost through radiation, while [6] states that in a typical fire scenario radiation accounts for 35% of the energy transport.

3.4. Outlet Boundary Condition

On a general basis, the geometry investigated would have no outlet since during the experiments the door of the garage was closed after the fire was lit. However, a standard closed metal sheet garage is far from being a watertight compartment so that the slightest pressure increase due to the rise in temperature of the air is immediately balanced by gas leakages. During the experiments it was noted that smoke was flowing out of the room from several spots, and in particular from the gaps along the door perimeter.

Thus, for simulation purposes, two $2\,cm \times 3\,m$ horizontal gaps on the front wall were used as outlet sections to enable gas leakages. These were located at the

ground level and at 2.9 m from the ground, that is, at the top and the bottom extremities of the garage door. The two gaps were repeated on the back wall. The gaps height was chosen small enough not to let fresh air in as long as the fire was lit and the room temperature rising, and large enough for the pressure rise in the room during heating to remain negligible.

3.5. Walls Boundary Condition

On the walls of the garage a Robin boundary condition is applied in which the reference ambient temperature is 15 °C. A global external heat transfer coefficient of 24 W/m² K is applied at the walls, with the exception of the floor were the coefficient is reduced to 4 W/m² K. The thermal emissivity of the walls and the floor is set to 0.9: even though the garage is made of metal sheets, at the time of the experiment the walls were already blackened by smoke from previous experiments.

3.6. Thermocouple Reading Correction

As mentioned, the thermocouples used for the experiments were non-shielded, this means the temperature readings collected during the experiments will be affected by some error. While this is likely negligible away from the flame, for the thermocouples in the flame region (TC 1, TC 2, TC 3, and TC 11) the temperature registered during the experiments may be underestimated up to a few hundred degrees. The correction of the temperature readings is not an easy task since several sources of error may be introduced in this operation.

In this work, thermocouple readings were corrected *a posteriori* following the bare-bead thermocouple model developed by Blevins and Pitts [44]. An additional term was included in order to account for unsteady effects. From the energy balance of the bead we have

$$h_{\text{gb}}\left(T_{\text{g}} - T_{\text{b}}\right) = \varepsilon_{\text{b}}\sigma\left(T_{\text{b}}^4 - T_{\infty}^4\right) + \frac{m_{\text{b}}c_{\text{b}}}{A_{\text{b}}}\frac{\text{d}T_{\text{b}}}{\text{d}t} \tag{8}$$

where T_{g} is the gas temperature, T_{b} the temperature read at the thermocouple bead, T_{∞} the average effective radiation temperature of the surrounding environment. h_{gb} is the convective heat transfer coefficient between the external gas flow and the bare thermocouple bead, ε_{b} the thermocouple bead emissivity, σ the Stefan-Boltzmann constant. m_{b}, c_{b}, and A_{b} are the bead mass, specific heat, and surface area.

The h_{gb} coefficient is estimated using Whitaker's correlation for external flow over a sphere [45]

$$\text{Nu} = 2 + \left(0.4\,\text{Re}^{0.5} + 0.06\,\text{Re}^{\frac{2}{3}}\right)\text{Pr}^{0.4} \tag{9}$$

with Nusselt, Reynolds, and Prandtl number given by

$$\text{Nu} = \frac{h_{gb}d_b}{k_g} \quad , \quad \text{Re} = \frac{\rho_g u_g d_b}{\mu_g} \quad , \quad \text{Pr} = \frac{c_{p,g}\mu_g}{k_g} \tag{10}$$

where d_b is the thermocouple bead diameter, and u_g the gas velocity in the neighbourhood of the thermocouple bead. k_g, ρ_g, μ_g, and $c_{p,g}$ are the thermal conductivity, the density, the dynamic viscosity, and the specific heat at constant pressure of the gas.

By solving Eq. (8) in terms of the corrected gas temperature T_g

$$T_g = T_b + \frac{\varepsilon_b \sigma}{h_{gb}}\left(T_b^4 - T_\infty^4\right) + \frac{m_b c_b}{h_{gb}A_b}\frac{dT_b}{dt} \tag{11}$$

is found. In order to solve this equation eleven parameters must be known, these are: the gas properties as functions of the temperature (ρ_g, μ_g, k_g, $c_{p,g}$), the thermocouple bead geometry and properties (d_b, ε_b, m_b, c_b, A_b), the gas velocity in the neighbourhood of the thermocouple bead (u_g), the radiation temperature of the surrounding environment (T_∞).

By neglecting the effect of combustion products, it is accepted that the gas is air and its properties are known. The thermocouple data is also known except for its emissivity that anyhow can be estimated within a reasonable accuracy. A typical value of 0.8 is suggested in [46] for dull, oxidized metal. Since no velocity data was gained from the experiments, information extrapolated from the simulations is used in its place. The same holds for the radiation temperature: the choice of a proper T_∞ is not straightforward because of the temporally and spatially varying environment, yet the incident radiation is available from the simulations from which its value can be derived.

To be noted that the unsteady term in Eq. (11) is found to be mostly negligible, growing marginally at the beginning of the simulation when temperature gradients with respect to time are larger. The radiative term, instead, can become much relevant but only in the flame region.

4. Results

In the following the results of the experiments and of the simulations are discussed and compared quantitatively in terms of temperature history at the thermocouples location, and qualitatively in terms of flame extension as recorded by the camera. Also some comment on the gas composition in the room as predicted by simulations is given.

### 4.1. Temperature History at the Thermocouple Locations

Figure 4 compares the temperature readings to the corresponding numerical predictions at six different thermocouple locations. The locations are chosen to be representative of the entire domain. In the figure, experimental results are reported together with numerical results from the three simulations. In general, the radia-
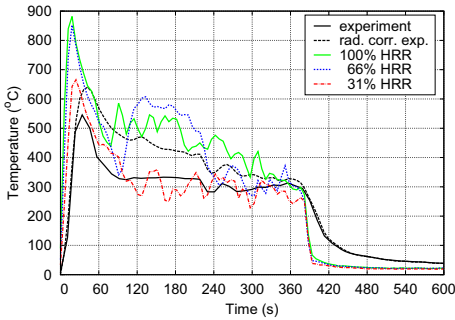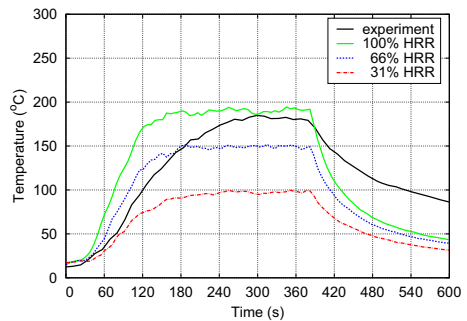
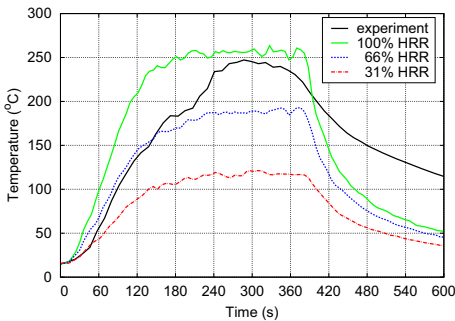(a) TC 1: x centred, y centred, $z=0.12$ m (flame region, above the pool surface)
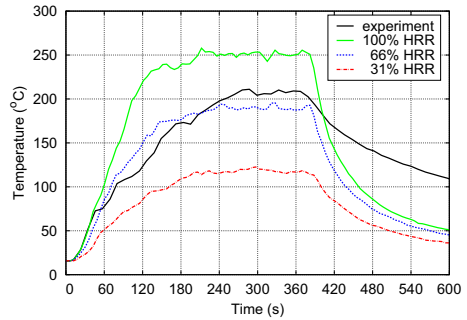
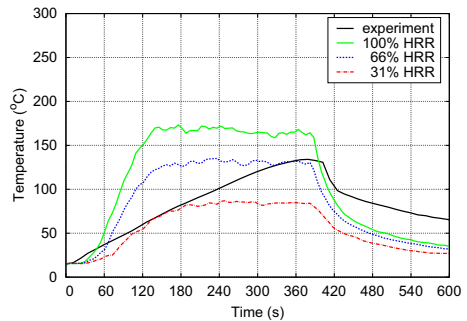(b) TC 5: x right of the panel, y centred, $z=3$ m
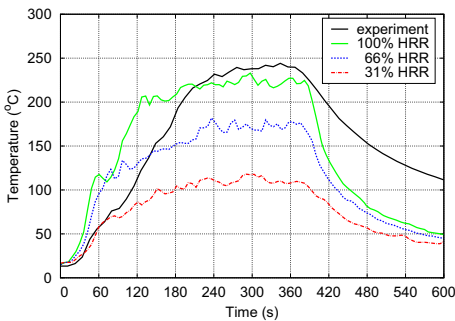
(c) TC 7: x centred, y centred, $z=2$ m

(d) TC 8: x at the wall, y centred, $z=1$ m

(e) TC 13: x centred, y behind the panel, $z=3$ m

(f) PTC 1: x centred, y in front of the panel, $z=0.5$ m

Figure 4. Experimental measurements versus numerical predictions for temperature at several thermocouple locations.

tion correction is small (<3°C on average) except for thermocouples located in the flame region where the correction can exceed 100°C, as expected. For this reason, the radiation corrected experimental temperature is reported only for TC 1.

Experimental data is collected every 11 s. Numerical data in the figure is collected every second and plotted on a 11 s moving average basis for the purpose of smoothing the oscillations. The matching between the numerical and the experi-

mental data is satisfactory as the temperature histories at the various locations is well reproduced.

Compared to CFD, all experimental results are characterised by reduced temperature gradients at all TC both during the initial room heating after the pool fire lighting, and during the final room cooling after the fire extinguishment. This is to be attributed to the thermocouple thermal inertia whose characteristic time, likely in the tens of seconds, can be written as

$$t_c = \frac{\rho c V}{hA} \tag{12}$$

where ρ is the bead material density, c its specific heat, V/A the volume to area ratio, and h the convective heat transfer coefficient. At PTC 1 (Figure 4f) the role of thermal inertia is particularly evident due to the larger probe size.

At TC 1, in the flame region, an initial temperature overshoot is caught both by experiments and simulations (Figure 4a). In the latter case, the temperature peak is sharper and occurs earlier in time. The temperature then settles and oscillates around an average value for the rest of the combustion process.

Among the other probes, the temperature trend is self-similar: at first it grows up to a rather stable value before dropping quickly after fire extinguishment. Temperature stability is reached in ≈ 2.5 minutes for the simulations and in ≈ 4.5 minutes during the experiments. The temperature reached depends primarily on the combustion efficiency (or on the HRR) and on the convective coefficient at the garage walls. From a simple energy balance, in fact, it is estimated that at the time of fire extinguishment more than 80% of the THR has been discharged through the walls, the rest accounting for the increased room temperature and, to a lesser extent, for the heat discharged with the hot gas flowing through the outlets.

The neighbourhood of the walls is subject to strong temperature gradients which translate, for instance, into the lower temperatures found at TC 8 compared to other thermocouples. In line with this, it must be pointed out that close to the walls the tiniest imprecision in the thermocouples positioning can result in non-negligible differences in the experimental temperature readings compared to the simulations. On the other hand, a minor error in the estimate of the wall thermal bouandary condition may result in non-negligible temperature offsets in the simulation.

Overall, the experimental results are compatible with an average combustion efficiency in the range between 66% and 100%, as shown in Figure 4.

Figure 5 shows the simulated temperature field right before the fire extinguishment on the $y = 0$ plane. Of course the temperature in the room rises with the combustion efficiency: while in Figure 5a a large portion of the room remains below 100°C in Figure 5c almost the whole room is above 200°C. It is interesting to note how in Figure 5c the extent of the flame (or better, the high temperature area above the pool) appears smaller in size when compared to the other figures. This is actually due to the temporary swaying of the flame behind the $y = 0$ plane level favoured by the lack of oxygen in the region.
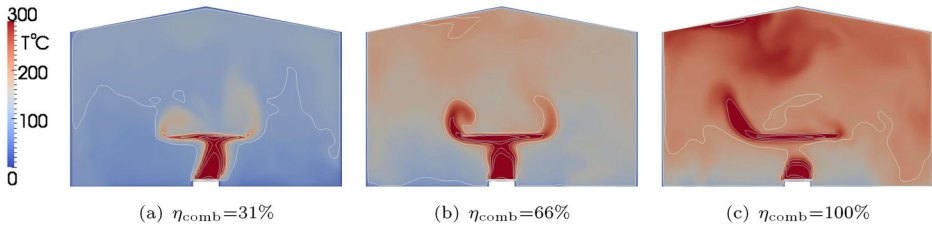
(a) η_{comb}=31%   (b) η_{comb}=66%   (c) η_{comb}=100%

Figure 5. Temperature field on the $y = 0$ plane at $t = 378$ s. Temperature is expressed in °C, the lines in the figures are contour lines traced every 100 degrees in the 100 to 500 °C range.

4.2. Average Gas Composition History in the Room

Figure 6 shows the gas average composition and total mass time history in the garage room computed from CFD simulations. Please consider that gas composition was not measured experimentally.

At $t = 0$ s the air density equals $1.211\,\text{kg/m}^3$ and the overall air mass in the room sums up to 110.49 kg. Over the first 2 min to 3 min after the pool fire is lit, as the air is heated, a large mass of gas is expelled from the room due to the lowering of its density (Figure 6a) while the internal pressure is essentially in equilibrium at any time with the outer environment. The mass flow rate at the outlet is up to 0.2 or 0.4 kg/s, depending on the combustion efficiency.

At $t = 379$ s the fluid density drops to 0.710, 0.784, and $0.901\,\text{kg/m}^3$ for the decreasing combustion efficiencies respectively. After the fire is extinguished and the room begins to cool down, the flow at the outlet is inverted and fresh air enters the room, also favouring its cooling in turn. At $t = 600$ s the gas mass within the domain is back to $\approx101.0\pm1.4$ kg for all the simulations.

For what concerns the average gas composition trend in the room (Figs. 6b–d), of course the nitrogen mass fraction is not subject to large variations in time (72.7 ± 2.2%), while things are different for oxygen and the combustion products. According to Eqs. (3–5), in fact, the oxygen consumption is of $3.512\,\text{kg}_{O_2}/\text{kg}_{C_7H_{16}}$ for $\eta_{\text{comb}} = 100$%, $2.555\,\text{kg}_{O_2}/\text{kg}_{C_7H_{16}}$ for $\eta_{\text{comb}} = 65$%, and $1.597\,\text{kg}_{O_2}/\text{kg}_{C_7H_{16}}$ for $\eta_{\text{comb}} = 31$%. At the end of the combustion process, the average oxygen mass fraction has dropped to 5.7%, 10.7%, and 15.9% for the three combustion efficiencies respectively. While the room is still rich in oxygen, the average heptane mass fraction stabilises quickly before dropping to zero as the combustion comes to an end. For the $\eta_{\text{comb}} = 100$% case, instead, the progressive oxygen depletion around the flame region and in the room leads to increased vaporised fuel mass fraction in the room; fraction that in any case remains very low (i.e. ≈250 ppm at most).

Figure 7 shows the oxygen and carbon dioxide mass fraction fields evolution after 2, 4, and 6 min from the fire ignition on the $y = 0$ plane for the $\eta_{\text{comb}} = 100$% case.
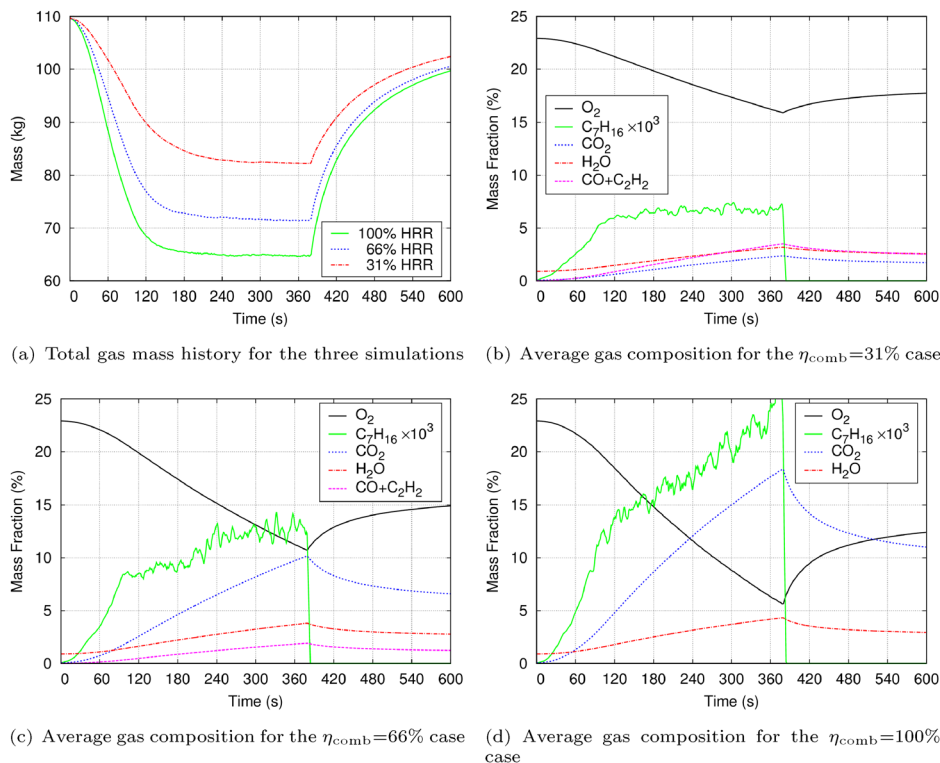
(a) Total gas mass history for the three simulations

(b) Average gas composition for the $\eta_{comb}=31\%$ case

(c) Average gas composition for the $\eta_{comb}=66\%$ case

(d) Average gas composition for the $\eta_{comb}=100\%$ case

Figure 6. Average gas composition and mass time history in the garage room after the simulations.

4.3. Flame Evolution

Figure 8 shows a few frames captured at different times by the camera during the experiment. After just a few minutes the flame is hidden by the large amount of smoke generated in the room; for this reason no image from the camera is reported after $t = 180\,s$. These images are compared to equivalent pictures taken from the simulations in which the extent of the flame is approximated by the iso-surface at $500°C$, in line with [47] where the iso-surface at $800\,K$ was used, since no flame is formally modelled by FireFOAM solver.

The image, thus, offers a qualitative view of the experimental and the numerical flame evolution in time. Even though high temperature and flame extension are not the same, they are correlated to each other. Similar images could have been extracted from the simulations if iso-surfaces of the radiation intensity were drawn.

The flame behaviour is quite variable due to its swaying in time, in particular at later combustion stages. At $t = 60\,s$ the flame is still quite stable and its extension limited to the area below the panel, with the flame touching the panel lower side. After two or three minutes the flame has grown so that tongues of fire spread
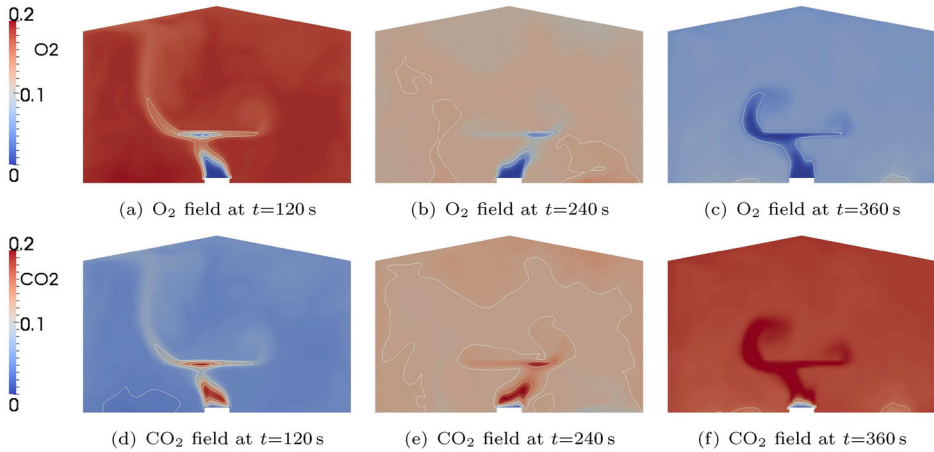
(a) O_2 field at $t=120$ s   (b) O_2 field at $t=240$ s   (c) O_2 field at $t=360$ s

(d) CO_2 field at $t=120$ s   (e) CO_2 field at $t=240$ s   (f) CO_2 field at $t=360$ s

Figure 7. Oxygen and carbon dioxide mass fraction fields evolution after 120, 240, and 360 s from the fire ignition on the y = 0 plane. The contour lines in the figures are traced every 0.04 in the 0.04 to 0.16 range. The figures refer to the $\eta_{\text{comb}} = 100\%$ simulation.

irregularly around and above the panel corners. According to simulations, a similar behaviour is kept up to the fire extinguishment due to the relatively large HRR of the fire.

5. Conclusions

Simulations of a pool fire in a large under-ventilated environment (namely, a closed garage) have been performed using the FireFOAM CFD solver included in OpenFOAM distribution to test the code capabilities in a challenging fire scenario. The results have been compared to experimental data collected in terms of temperature history at several locations in the domain.

A fairly good agreement was found between experimental and numerical data, but only at the cost of an artificial and iterative tuning of several parameters in the computational model, such as the heat release rate history, the efficiency of the combustion, and the heat transfer boundary conditions at the walls. These are not secondary aspects and the uncertainty in their definition somewhat mines the general predictive capability of these models. Nonetheless, results in terms of temperature field evolution and flame extension and behaviour are acceptable, also considering the standard numerical modelling features adopted.

The use of CFD simulations in the field of fire safety engineering for sure is a promising tool able to provide large amounts of information. However, it is still subject to several critical issues and must be used with caution, since accurate models of the physical and the chemical processes involved either do not exist, have no general validity, or are way too expensive from the computational point of view to be applied to full-scale scenarios in practice.
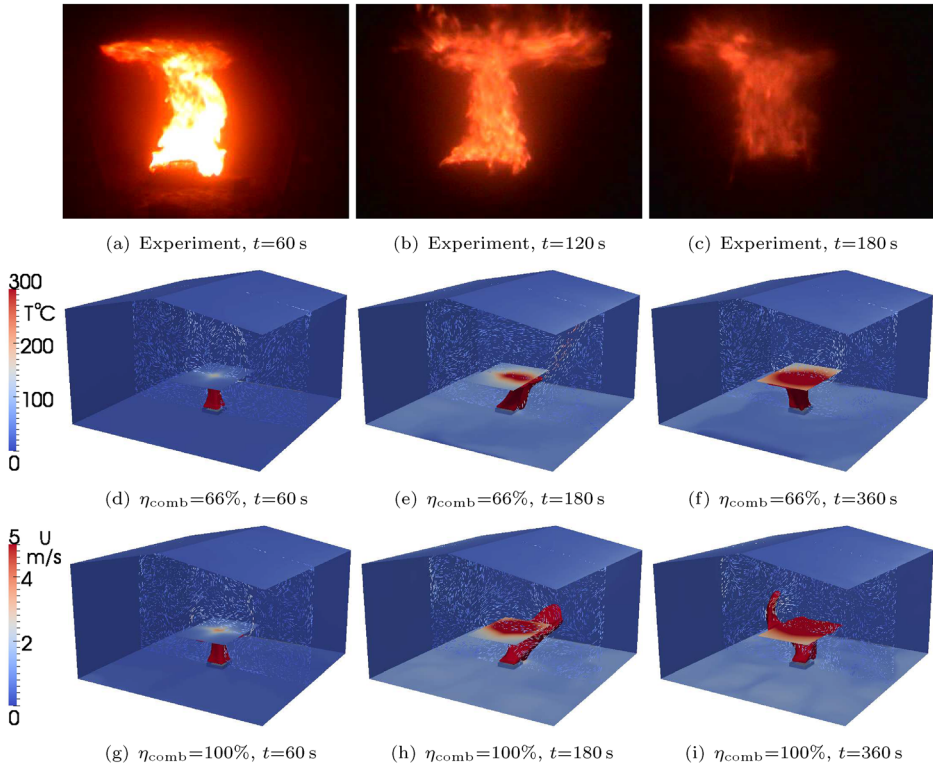
(a) Experiment, $t=60\,\mathrm{s}$ (b) Experiment, $t=120\,\mathrm{s}$ (c) Experiment, $t=180\,\mathrm{s}$

(d) $\eta_{\mathrm{comb}}=66\%$, $t=60\,\mathrm{s}$ (e) $\eta_{\mathrm{comb}}=66\%$, $t=180\,\mathrm{s}$ (f) $\eta_{\mathrm{comb}}=66\%$, $t=360\,\mathrm{s}$

(g) $\eta_{\mathrm{comb}}=100\%$, $t=60\,\mathrm{s}$ (h) $\eta_{\mathrm{comb}}=100\%$, $t=180\,\mathrm{s}$ (i) $\eta_{\mathrm{comb}}=100\%$, $t=360\,\mathrm{s}$

Figure 8. Flame evolution: experiment versus $\eta_{\mathrm{comb}} = 66\%$ and $\eta_{\mathrm{comb}} = 100\%$ simulations. For the experiment, images taken from the camera are reported. For the simulations, temperature fields on the walls and velocity vectors on the $y = 0$ plane coloured by velocity magnitude are drawn. The flame is approximated by the iso-surface at 500°C.

With regard to the case study investigated here, it has been discussed how a general model for computing the burning rate from a pool fire is missing, and how this can be estimated *a posteriori* on the basis of experimental radiative heat flux readings extrapolated from a plate thermocouple. Further, an accurate analysis of the chemistry involved in the combustion is generally out of reach due to computational reasons. Nonetheless, this is deemed acceptable in fire safety engineering where the interest is on the effects of the fire thermal load in an environment, rather than on tracking the chemistry kinetic and the combustion products formation in detail. In any case, due to the lack of proper combustion and soot formation models in the simulations, a gross chemical reaction had to be tuned iteratively to model combustion global effects at best. Finally, the choice of a proper heat transfer boundary condition at the walls is not always straightforward. Nonetheless, as this represents the main thermal energy sink of the system,

its choice can really make a difference on the predicted temperature field in confined fires.

Acknowledgements

Funding

Declarations

Conflict of interest The authors declare no conflict of interest

Open Access

References

1. Sinai Y (2000) Exploratory CFD modelling of pool fire instabilities without cross-wind. Fire Saf J 35:51–61. https:10.1016/S0379-7112(00)00011-4
2. Xue H, Ho J, Cheng Y (2001) Comparison of different combustion models in enclosure fire simulation. Fire Saf J 36:37–54. https:10.1016/S0379-7112(00)00043-6
3. Zang W, Hamer A, Klassen M et al (2002) Turbulence statistics in a fire room model by large eddy simulation. Fire Saf J 37:721–752. https:10.1016/S0379-7112(02)00030-9
4. Kim S, Ryou H (2003) An experimental and numerical study of fire suppression using a water mist in an enclosure. Build Environ 38:1309–1316. https:10.1016/S0360-1323(03)00134-3
5. Maragkos G, Merci B (2020) On the use of dynamic turbulence modelling in fire applications. Combust Flame 216:9–23. https:10.1016/j.combustflame.2020.02.012

6. McGrattan K, Floyd J, Forney G, et al (2003) Improved radiation and combustion routines for a large eddy simulation fire model. In: Evans D (ed) 7th international symposium on fire safety science – IAFSS, pp 827–838

7. Yeoh G, Yuen R, Lo S et al (2003) On numerical comparison of enclosure fire in a multi-compartment building. Fire Saf J 38:85–94. https:10.1016/S0379-7112(02)00032-2

8. Zhao F, Yang W, Yu W (2020) A progress review of practical soot modelling development in diesel engine combustion. J Traffic Transp Eng 7(3):269–281. https:10.1016/j.jtte.2020.04.002

9. Wang C, Liu H, Wen J (2018) An improved PaSR-based soot model for turbulent fires. Appl Therm Eng 129:1435–1446. https:10.1016/j.applthermaleng.2017.10.129

10. Deckers X, Haga S, Tilley N et al (2013) Smoke control in case of fire in a large car park: CFD simulations of full-scale configurations. Fire Saf J 57:22–34. https:10.1016/j.firesaf.2012.02.005

11. Wu B, Roy S, Zhao X (2020) Detailed modelling of a small-scale turbulent pool fire. Combust Flame 214:224–237. https:10.1016/j.combustflame.2019.12.034

12. Lin C, Ferng Y, Hsu W (2009) Investigating the effect of computational grid sizes on the predicted characteristics of thermal radiation for a fire. Appl Therm Eng 29:2243–2250. https:10.1016/j.applthermaleng.2008.11.010

13. Le V, Marchand A, Verma S et al (2019) Simulation of a turbulent line fire with a steady flamelet combustion model coupled with models for non-local and local gas radiation effects. Fire Saf J 106:105–113. https:10.1016/j.firesaf.2019.04.011

14. Liu F, Consalvi JL, Nmira F (2023) The importance of accurately modelling soot and radiation coupling in laminar and laboratory-scale turbulent diffusion flames. Combust Flame 258:112573. https:10.1016/j.combustflame.2022.112573

15. Maragkos G, Beji T, Merci B (2019) Towards predictive simulations of gaseous pool fires. Proc Combust Inst 37(3):3927–3934. https:10.1016/j.proci.2018.05.162

16. Domino S, Hewson J, Knaus R et al (2021) Predicting large-scale pool fire dynamics using an unsteady flamelet- and large-eddy simulation-based model suite. Phys Fluids 33(8):085109. https:10.1063/5.0060267

17. Hopkin C, Spearpoint M, Hopkin D (2019) A review of design values adopted for heat release rate per unit area. Fire Technol 55(5):1599–1618. https:10.1007/s10694-019-00834-8

18. Hasib R, Kumar R, Shashi et al (2007) Simulation of an experimental compartment fire by CFD. Build Environ 42:3149–3160. https:10.1016/j.buildenv.2006.08.002

19. Nasr A, Suard S, El-Rabii H et al (2011) Fuel mass-loss rate determination in a confined and mechanically ventilated compartment fire using a global approach. Combust Sci Technol 183:1342–1359. https:10.1080/00102202.2011.596174

20. Novozhilov V, Koseki H (2004) CFD prediction of pool fire burning rates and flame feedback. Combust Sci Technol 176:1283–1307. https:10.1080/00102200490457484

21. Pope N, Bailey C (2006) Quantitative comparison of FDS and parametric fire curves with post-flashover compartment fire test data. Fire Saf J 41:99–110. https:10.1016/j.firesaf.2005.11.002

22. Amouzandeh A, Shrestha S, Zeiml M, et al (2010) Design of a computational-fluid-dynamics tool for the simulation of pre-specified fire scenarios in enclosures. In: Pereira J, Sequeira A (eds) V European conference on computational fluid dynamics – ECCOMAS CFD 2010

23. Suard S, Lapuerta C, Babik F et al (2011) Verification and validation of a CFD model for simulations of large-scale compartment fires. Nucl Eng Des 241:3645–3657. https:10.1016/j.nucengdes.2011.08.012

24. Wang H (2009) Numerical study of under-ventilated fire in medium-scale enclosure. Build Environ 44:1215–1227. https:10.1016/j.buildenv.2008.09.011

25. Wang Y, Chatterjee P, de Ris J (2009) Large eddy simulation of fire plumes. Proc Combust Inst 33:2473–2480. https:10.1016/j.proci.2010.07.031

26. Maragkos G, Rauwoens P, Merci B (2012) Application of FDS and fireFOAM in large eddy simulations of a turbulent buoyant helium plume. Combust Sci Technol 184:1108–1120. https:10.1080/00102202.2012.664002

27. Almeida Y, Lage P, Silva L (2015) Large eddy simulation of a turbulent diffusion flame including thermal radiation heat transfer. Appl Therm Eng 81:412–425. https:10.1016/j.applthermaleng.2015.02.027

28. Myers T, Trouvé A, Marshall A (2018) Predicting sprinkler spray dispersion in FireFOAM. Fire Saf J 100:93–102. https:10.1016/j.firesaf.2018.07.008

29. Grange N, Chetehouna K, Gascoin N et al (2018) One-dimensional pyrolysis of carbon based composite materials using FireFOAM. Fire Saf J 97:66–75. https:10.1016/j.firesaf.2018.03.002

30. Bordes A, Danilov D, Desprez P et al (2022) A holistic contribution to fast innovation in electric vehicles: an overview of the DEMOBASE research project. ETransportation 11:100144. https:10.1016/j.etran.2021.100144

31. Jang D, Hu L, Jiang Y et al (2010) Comparison of FDS predictions by different combustion models with measured data for enclosure fires. Fire Saf J 45:298–313. https:10.1016/j.firesaf.2010.06.002

32. Prétrel H, Suard S (2023) Investigation of the fire mass loss rate in confined and mechanically ventilated enclosures on the basis of a large-scale under-ventilated fire test. Fire Saf J 141:103962. https:10.1016/j.firesaf.2023.103962

33. Prétrel H, Bouaza L, Suard S (2021) Multi-scale analysis of the under-ventilated combustion regime for the case of a fire event in a confined and mechanically ventilated compartment. Fire Saf J 120:103069. https:10.1016/j.firesaf.2020.103069

34. Rasoulipour S, Delichatsios M, Fleischmann C et al (2020) Experimental investigation of underventilated fires in enclosures with two front vertical openings and occurrence of smoke explosions. Fire Saf J 116:103176. https:10.1016/j.firesaf.2020.103176

35. Chotzoglou K, Asimakopoulou E, Zhang J (2019) An experimental investigation of burning behaviour of liquid pool fire in corridor-like enclosures. Fire Saf J 108:102826. https:10.1016/j.firesaf.2019.102826

36. Vilfayeau S, Ren N, Wang Y et al (2015) Numerical simulation of under-ventilated liquid-fueled compartment fires with flame extinction and thermally-driven fuel evaporation. Proc Combust Inst 35(3):2563–2571. https:10.1016/j.proci.2014.05.072

37. Betting B, Varea E, Godard G et al (2019) Experimental and numerical studies of smoke dynamics in a compartment fire. Fire Saf J 108:102855. https:10.1016/j.firesaf.2019.102855

38. Lafdal B, Djebbar R, Boulet P et al (2022) Numerical study of the combustion regimes in naturally-vented compartment fires. Fire Saf J 131:103604. https:10.1016/j.firesaf.2022.103604

39. Smagorinsky J (1963) General circulation experiments with the primitive equations. I The basic experiment. Month Wea Rev 91:99–164

40. Wang J, Zhang R, Wang Y et al (2023) Experimental study on combustion characteristics of pool fires in a sealed environment. Energy 283:128497. https:10.1016/j.energy.2023.128497

41. Yuan M, Chen B, Li C et al (2013) Analysis of the combustion efficiencies and heat release rates of pool fires in ceiling vented compartments. Procedia Eng 62:275–282. https:10.1016/j.proeng.2013.08.065

42. Pitts W (1995) The global equivalence ratio concept and the formation mechanisms of carbon monoxide in enclosure fires. Prog Energ Combust 21(3):197–237. https:10.1016/0360-1285(95)00004-2

43. Ingason H, Wickström U (2007) Measuring incident radiant heat flux using the plate thermometer. Fire Saf J 42:161–166. https:10.1016/j.firesaf.2006.08.008

44. Blevins L, Pitts W (1999) Modeling of bare and aspirated thermocouples in compartment fires. Fire Saf J 33:239–259. https:10.1016/S0379-7112(99)00034-X

45. Whitaker S (1972) Forced convection heat transfer correlations for flow in pipes, past flat plates, single cylinders, single spheres, and for flow in packed beds and tube bundles. AIChE J 18:361–371. https:10.1002/aic.690180219

46. Incropera F, Dewitt D, Bergman T et al (2006) Fundamentals of heat and mass transfer, 6th edn. Wiley, Hoboken

47. Yi H, Feng Y, Park H et al (2020) Configuration predictions of large liquefied petroleum gas (LPG) pool fires using CFD method. J Loss Prevent Proc 65:104099. https:10.1016/j.jlp.2020.104099